JMEPEG (2020) 29:3551–3559
https://doi.org/10.1007/s11665-020-04714-z

1059-9495/$19.00

Quantitative Analysis of Microstructural Refinement in Simulated Carburized Microstructures

M. Agnani, O.L. DeNonno, K.O. Findley, and S.W. Thompson

(Submitted December 5, 2019; in revised form February 17, 2020; published online March 9, 2020)

Microstructure refinement strategies in simulated carburized microstructures were evaluated because of their potential for improving the fatigue performance of case-carburized components. Commercial 52100 steel was used to simulate the high-carbon content in the case. Specimens were subjected to various thermal treatments in a quenching dilatometer. Reheating cycles to austenitizing temperatures were evaluated with respect to both prior austenite grain size (PAGS) and associated martensite and retained austenite (RA) refinement. Quantitative stereological measurements were performed to evaluate the microgeometry of plate martensite and the size distribution of RA regions. Decreasing the reheating temperature resulted in finer PAGS, and multiple reheating cycles resulted in a narrower PAGS distribution. Refinement in PAGS led to a reduction in martensite plate size and finer distribution of RA. Additionally, interrupted quenching below martensite start (M_S) temperature was evaluated. This processing route results in a refinement of martensite plates and more stable RA. The stabilization of austenite may be mechanical or chemical in nature, owing to the deformation of austenite during primary transformation, or due to partitioning of carbon into austenite similar to quenching and partitioning steels.

Keywords carburizing, martensite transformation, microstructure refinement, retained austenite, stereology, steel heat treatment

1. Introduction

Carburized steel components find applications in vehicle powertrains, machines, and power generation equipment where high strength is required in combination with good fatigue resistance (Ref 1). These desirable properties can be attributed to complex microstructures consisting of plate martensite and retained austenite (RA) in the carbon-rich case and low-carbon microstructures in the core. There is a gradient of carbon concentration and hence RA content, microstructure, and hardness along the depth of the components (Ref 2). It is imperative to advance our understanding of the characteristics of carburized microstructures for optimized processing and performance of drive-train components.

Wise and Matlock (Ref 3) performed a statistical analysis to correlate microstructural variables with bending-fatigue endurance limits of carburized steels. Case grain size is the most critical parameter that influences endurance limits in carburized components (Ref 3). Finer austenite grains result in improved fatigue lives, which is hypothesized to be due to refinement of martensite plates, phosphorus dilution along austenite grain boundaries, and lower susceptibility to quench microcracking (Ref 2). Apple and Krauss (Ref 4) showed that refinement of prior austenite grains in the case regions using reheating cycles led to improvements in fatigue performance. During reheating to elevated temperatures, austenite grains nucleate and grow at prior austenite grain boundaries (PAGBs) and at martensite/austenite interfaces. Because of the multitude of grain nucleation sites, finer prior austenite grain size (PAGS) can be achieved. Krauss (Ref 2) reported that triple reheating treatments led to a three times reduction in PAGS of carburized 4320 steel throughout the carburized case.

The mechanism of transformation of martensite from austenite is displacive and occurs at about the speed of sound in steel (Ref 5). As a result, it is experimentally complicated to study, resolve, and interpret the nucleation and growth events. Two common martensite morphologies are found in steels: lath and plate, where the latter is common in high-carbon microstructures. Three different modes of kinetics are predominantly discussed in the literature: athermal, isothermal, and burst kinetics (Ref 6). The extensive literature on isothermal and burst kinetics of martensite growth exists for Fe-Mn-Ni systems (Ref 7, 8). Athermal martensite is usually observed in low-alloy carbon steel (Ref 5). In most steels, the transformation of austenite to martensite proceeds upon lowering the temperature below the martensite start temperature, M_s, and is not a function of time (because of rapid rate of transformation), hence the name athermal. The transformation extends to a temperature range between M_s (martensite start) and a certain temperature M_f (martensite finish) below which no transformation takes place even in the case of the presence of untransformed austenite. Under isothermal conditions at a temperature between M_s and M_f, the transformation rate rapidly slows, but increases upon further lowering of temperature (Ref 6). The kinetics of martensite transformation depends on the nucleation of martensite plates, as the plates grow rapidly thereafter. Therefore, the extent of transformation is dictated by the undercooling below the M_S

This article is an invited submission to JMEP selected from presentations at the 30th Heat Treating Society Conference and Exposition held October 15-17, 2019, in Detroit, Michigan, and has been expanded from the original presentation.

M. Agnani, O.L. DeNonno, K.O. Findley, and **S.W. Thompson**, Advanced Steel Processing and Products Research Center, Colorado School of Mines, Golden, CO 80401. Contact e-mail: magnani@mymail.mines.edu.

temperature (thermodynamic driving force for nucleation) and not on the time available for growth (athermal) (Ref 7). Olson and Cohen (Ref 9, 10) suggest that preexisting defects in fcc (austenite) serve as favorable nucleation sites for martensite. Recent molecular dynamics simulations also discuss the thermodynamics and kinetics of several atomistic transformation mechanisms responsible for nucleation of martensite on defects in the austenite (Ref 11). The structure of the prior austenite grain (size and density of defects) is thus one of the most important factors that influence the athermal martensite transformation kinetics (Ref 12).

Previously, researchers have studied the effect of interrupted quenching on evolution of microstructure in commercial steels. In low-carbon TRIP (transformation induced plasticity) steels containing alloying additions that suppress carbide precipitation, carbon can partition from supersaturated martensite into untransformed austenite upon aging during interrupted quenching (Ref 13). The carbon-rich untransformed austenite can thus be chemically stabilized. In a Fe-0.8C high-carbon steel, Van Bohemen et al. (Ref 5) showed that partial bainite transformation during interrupted quenching stabilizes austenite. A volume change associated with bainite and martensite transformation deforms and strengthens the surrounding austenite, thereby resulting in mechanical stabilization of RA. Interrupted quenching can thus chemically or mechanically stabilize the austenite and affect the subsequent martensite transformation.

In several published papers, stereological methods have been used to investigate and mathematically formalize the mechanisms and kinetics of martensite formation and to characterize the plate martensite and RA microstructure (Ref 14-16). Previous stereological studies also suggest that PAGBs strongly influence the nucleation of martensite. In the early stages of transformation, Chang et al. (Ref 14) observed that in coarse-grained microstructures a greater fraction of martensite plates nucleate at PAGBs than in fine-grained samples. However, in the later stages of transformation, no differences were observed for the autocatalytic tendencies of the plates (i.e., nucleation of new plates on existing plates) at PAGBs and within austenite grains (Ref 14). PAGS also influences the so-called spread of martensite (Ref 16). The spread of transformation kinetics is different for large and small grains. Large grains promote uniform spread and fill-in of martensite transformation, whereas small grains show partially transformed clusters of grains and in the later stages of the transformation, plate formation gradually spreads in all austenitic grains (Ref 17).

PAGS influences both the martensite transformation and the endurance limits in carburized components. However, the link between martensitic microstructure and fatigue performance is not well established. In this investigation, stereological methods are employed to provide a quantitative basis for the evaluation of refinement in plate-martensite and RA constituents associated with thermal cycling and step quenching . Additionally, step quenching is introduced as a potential heat treatment strategy to stabilize RA in high-carbon plate-martensite and austenite microstructures.

2. Experimental Procedures

2.1 Materials

In this study, commercially available high-carbon 52100 bar steel was used as a simulation alloy for the case region of carburized components since austenitizing and quenching heat treatments result in plate martensite and RA microstructures, similar to a case region of a carburized components. The composition of the steel is given in Table 1. Cylindrical samples with a diameter of 4 mm and length of 10 mm were machined out of an 82.6-mm-diameter bar from the half-radius position. The specimens were used to perform controlled heat treatments using a TA Instruments Type 805L quenching dilatometer. Two heat treatments, namely thermal cycling and step quenching, are described below.

2.2 Thermal Cycling

The as-received microstructure consisted of pro-eutectoid cementite along PAGBs and pearlite colonies with an initial colony size of 68.9 ± 3.9 μm. Using dilatometry, the A_{C1} and A_{CM} temperatures were determined to be 780, and 793 °C, respectively. All samples were heated to 1000 °C at 5 °C·s^{-1} to ensure complete austenitization and carbide dissolution (constant for all subsequent heat treatments), held isothermally for 100 s and quenched to room temperature at 10 °C·s^{-1} to form a martensitic microstructure similar to that present in the case of a carburized microstructure. In the subsequent thermal cycling step, samples were reheated to three different austenitizing temperatures, 900, 1000, or 1100 °C, held isothermally for 100 s and quenched at 20 °C·s^{-1} to ensure martensite formation (hereby called RH900, RH1000, and RH1100 samples, respectively). Further, to study the influence of time, a short reheating treatment was performed at 900 °C for 1 s. Up to three short reheating cycles (designated as RHS—*n* where *n* is number of cycles) at 900 °C for 1 s (with an interval of 60 s in between subsequent cycles) were also carried out to study the evolution of PAGS during thermal cycling. Figure 1(a) shows summary of thermal cycles.

2.3 Step Quenching

To perform step quenching studies, samples were heated to 1000 °C at a heating rate of 5 °C·s^{-1} and isothermally held for 100 s under vacuum. This time and temperature combination ensured a fully austenitic microstructure with carbide dissolution. The samples were argon gas quenched to 100 °C (M_s = 142° C) with a cooling rate of 10 °C·s^{-1}, held isothermally for 1000 s, and subsequently quenched to room temperature at 10 °C·s^{-1} to form a martensitic microstructure similar to that present in the case of a carburized microstructure (Fig. 1b).

2.4 Stereological Analysis

Cross sections of samples were hot mounted in bakelite and polished using standard metallographic procedures. Samples were etched with saturated picric acid to reveal the PAGBs and with 2 pct nital to quantify the martensite plates and RA sizes. The Abrams three-circle method was used to evaluate the PAGS of samples from picral-etched specimens according to ASTM E112. More than 400 prior austenite grains were sampled for measurement of PAGS. Polished cross sections were also etched with 2 pct nital to reveal plate martensite and RA microstructures. Stereological measurements of the martensite microgeometry were performed on scanning electron micrographs by standard stereological techniques such as point counting and lineal intercept counting (Ref 18).

Microstructures in metals and alloys contain three-dimensional features (such as precipitates), two-dimensional surfaces

Table 1 Composition of 52100 steel (in wt pct)

C	Mn	Si	Ni	Cr	Mo	V	Al	N	S	P	Cu	Fe
1.00	0.35	0.26	0.13	1.40	0.05	0.004	0.024	0.006	0.006	0.015	0.17	Bal.

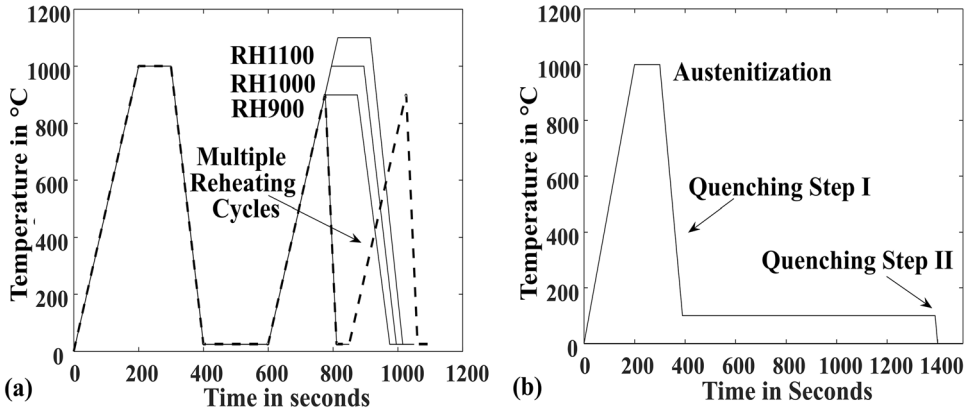

Fig. 1 Schematic diagram showing thermal history during (a) thermal cycling and (b) step quenching

(such as grain boundaries), and one-dimensional linear elements (such as dislocations). During metallographic analysis of two-dimensional cross sections, these microstructural features manifest as area sections, linear traces, and points in the plane of the observation, respectively (Ref 19). Probability and statistics-based stereological methods provide relationships between three-dimensional features of the microstructure and the two-dimensional observable properties of the micrographs (Ref 19). Conventional notations used in stereology and fundamental relationships (Eq 1-3) are discussed below. The derivations of these equations and a discussion of their accuracy are provided elsewhere (Ref 18, 19).

The notation used here, and in the literature, consists of a geometrical element 'E' and a geometrical dimension 'D'. The symbol E_D represents the quantity of E per unit dimension D; for example, N_V represents the number of features per unit volume. Inaccessible three-dimensional features like S_V or L_V, where S is surface area, V is volume and L is length, can be expressed in terms of two-dimensional quantities using mathematical relationships (Ref 18), some of which are listed below.

$$V_V = A_A = L_L = P_P \quad \text{(Eq 1)}$$

$$S_V = \left(\frac{4}{\pi}\right) L_A = 2P_L \quad \text{(Eq 2)}$$

$$L_V = 2P_A \quad \text{(Eq 3)}$$

where P, L, and A are point, length, and area, respectively.

Figure 2 schematically shows the evaluated stereological quantities: surface area per unit volume of martensite midplane (S_V^{MID}) and length per unit volume of midplane periphery (L_V^{MID}). Chen and Winchell proposed a correlation between shape-independent stereological features and the morphological aspects of plate martensite. In this study, two parameters were studied: t_{avg} and r_{avg} (Ref 14).

$$t_{\text{avg}} = V_V / S_V^{\text{MID}} \quad \text{(Eq 4)}$$

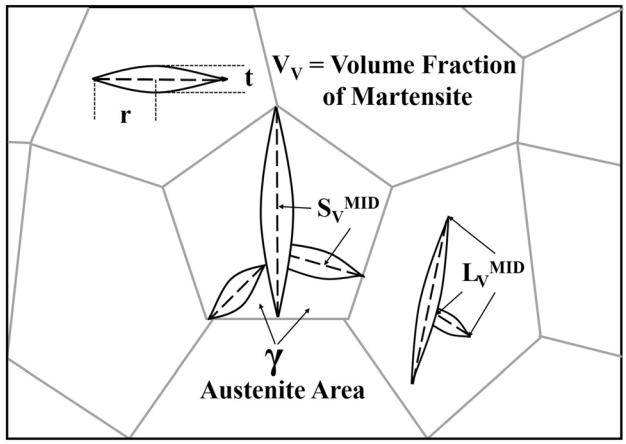

Fig. 2 A schematic drawing showing various stereological quantities measured during the investigation

$$r_{\text{avg}} = 2S_V^{\text{MID}} / L_V^{\text{MID}} \quad \text{(Eq 5)}$$

The t_{avg} is the average thickness of martensite plates weighted by midplane surface area (S_V^{MID}), r_{avg} is the average distance between the center of the plate and its periphery along the midplane, and V_V is the volume fraction of martensite (see Fig. 2). Hereby, r_{avg} will be referred to as the average martensite plate radius. Three-dimensional quantities in Eq 4 and 5 can be expressed in terms of two-dimensional properties using Eq 1-3.

$$t_{\text{avg}} = P_P / 2P_L^{\text{MID}} \quad \text{(Eq 6)}$$

$$r_{\text{avg}} = 2P_L^{\text{MID}} / P_A^{\text{MID}} \quad \text{(Eq 7)}$$

The point fraction of martensite, P_B, was determined by overlaying a grid of points on a microstructure and calculating the fraction of points lying within martensitic regions. P_L^{MID}

was determined by overlaying parallel lines on the microstructures and calculating the number of intersections between test lines and midribs per unit length of test line. P_A^{MID} was determined by counting the number of martensite plate ends per unit area of the microstructure.

To analyze the size distribution of RA constituents in microstructures, image processing was performed using MIPAR software. Using thresholding, areas of austenitic regions were identified in 2-D planes and their circular equivalent diameters were determined. The size distribution of the RA constituents per unit area was determined, given by $(N_A)_i$, as the number of RA constituents in each class interval, i, with diameter D_i. The average RA constituent diameter, D_{avg}, is given by

$$D_{avg} = \frac{1}{N_V}\left(\sum (N_V)_i D_i\right) \quad \text{(Eq 8)}$$

where $(N_V)_i$ is the number of constituents per unit volume in each class interval. N_V is not a measurable quantity in micrographs; however, it can be correlated with N_A by considering the probability of the test plane sectioning the RA constituents. The Schwartz-Saltykov method was employed to determine the RA constituent size distribution $(N_V)_i$ (Ref 18). The method was originally proposed for a poly-dispersed system of spheres, with inaccuracies resulting from non-spherical shapes. However, reasonable trends can be determined for equiaxed and spheroidal particles with this analysis assuming isotropic and uniformly scattered distribution of particles (Ref 18). Takahashi and Suito (Ref 20) evaluated the accuracy of the Schwartz-Saltykov method and found that the histogram of size distribution of particles was independent of the number of intervals, even for a small number of intervals. Thus, in this study, the analysis of RA sizes will be based on the size distribution histograms.

3. Results and Discussion

Stereological analysis was performed on microstructures developed using thermal cycling and step quenching. The results of PAGS, plate martensite, and RA sizes subjected to various thermal cycles are presented. Additionally, martensite microgeometry of step-quenched microstructures is compared with direct-quenched microstructures.

3.1 Thermal Cycling–Prior Austenite Grain Size

Figure 3 shows a light micrograph of a cross section of the RH1000 sample etched with saturated picric acid. The PAGBs are prominent, and the martensite–RA substructure is visible in certain regions too. The RH1000 sample showed significant microstructural banding of grain sizes possibly due to alloy segregation and compositional banding during prior processing. The narrow bands consisting of significantly smaller PAGS were avoided for stereological measurements. A small fraction of large carbides remained undissolved along PAGBs for all conditions. However, small carbides dissolved during reheating, and no grain pinning effect is expected from the remaining coarse carbides.

Figure 4 shows the prior austenite grain sizes as a function of reheating temperatures. Error bars represent the standard deviation in PAGS determined form different micrographs.

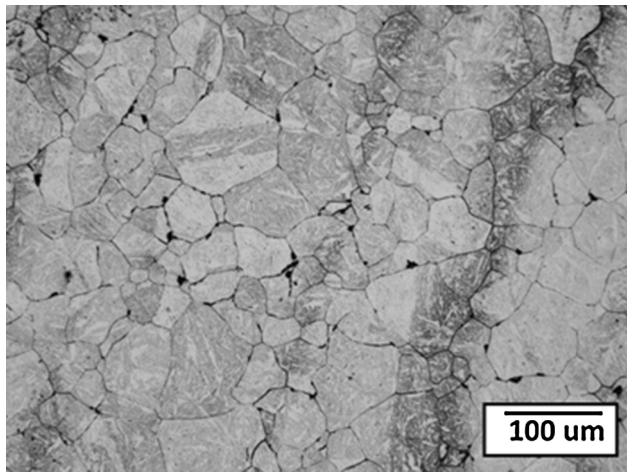

Fig. 3 Light micrograph of RH1000 sample, etched with saturated picric acid

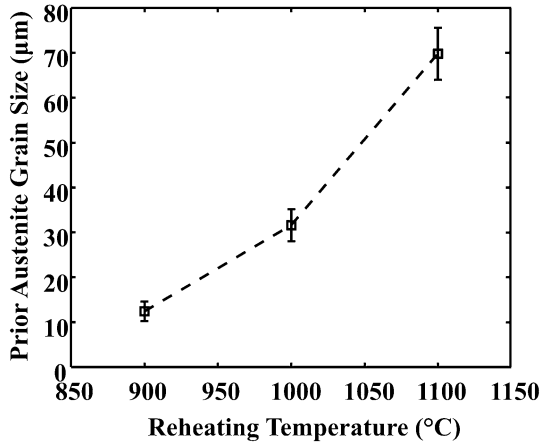

Fig. 4 Prior austenite grain size as a function of the reheating temperature during thermal cycling (isothermal holding of 100 s). More than 400 prior austenite grains were sampled to determine the PAGS for each condition

Reheating to higher temperatures leads to coarser PAGS. During reheat treatments, austenite reversion takes place, where austenite grains nucleate and grow on PAGBs and at martensite/austenite interfaces. They subsequently impinge against one another resulting in fine austenitic grains. However, during isothermal holding at elevated temperatures, grain growth subsequently occurs. Larger grains grow at the expense of smaller grains to reduce the grain boundary area of the microstructures.

Grain growth kinetics plays an important role in the final PAGS. Figure 5 shows the cumulative distribution function (CDF) of grain boundary intercept length for microstructures produced by multiple reheating cycles. For an austenite reversion cycle of 1 s at 900 °C, a significantly smaller final PAGS of 5.89 ± 0.48 μm was obtained, less than half the value for a 100 s hold at 900° C (RH900). It was observed that subsequent thermal cycling at 900°C did not alter the average grain sizes significantly; however, for multiple reheat cycles, the grain-size distribution became narrower. The triple reheated sample has a steeper CDF curve as compared to the single reheated sample, indicating a lower standard deviation in grain

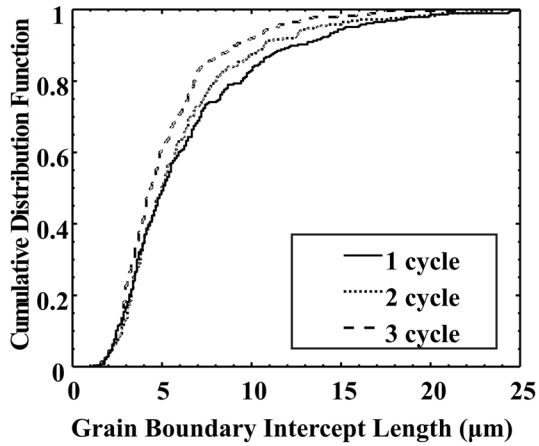

Fig. 5 Cumulative distribution function plots for grain boundary linear intercepts of microstructures produced by thermal cycling (900 °C and 1 s) subjected to multiple austenite reversion cycles

size in the triple reheated specimen. Roughly 20 pct of the lineal intercepts in RHS-1 are greater than 10 μm in length, while in RHS-3 less than 10 pct of the intercepts are greater than 10 μm. Lineal intercepts as large as 24.8 μm were observed for the RHS-1 sample. Crack nucleation during fatigue in carburized components can occur via intergranular fracture along PAGBs, and larger grains can serve as larger, more detrimental crack nucleation sites and may act as the weak link controlling fatigue performance. The difference in CDF between reheat conditions indicates that there are fewer large grains after subsequent thermal cycles. It is hypothesized that improved fatigue lives result from this narrower grain size distribution.

3.2 Thermal Cycling–Martensite Microgeometry

Figure 6 shows a representative electron micrograph from the RH1000 microstructure etched with 2 pct nital. The dark regions correspond to martensite, whereas the light regions are RA. The high-carbon martensite has plate morphology with varying sizes of martensite plates and RA encapsulated in between. Different microconstituents namely plate martensite (α') and retained austenite (γ) microconstituents are labeled. Midribs of some martensitic plates are indicated using white lines. The stereological features S_V^{MID} and L_V^{MID} (measured in terms of midplane periphery points per unit area, indicated by black circles) are also schematically highlighted. The stereological results are summarized in Table 2.

Figure 7(a) and (b) shows the trends in average martensite plate thickness and radius as a function of PAGS where the error bars represent the standard deviation in values obtained from different micrographs. All three conditions contain approximately 70 pct martensite by volume, and thus a similar degree of austenite partitioning can be assumed. Therefore, it is reasonable to quantitatively compare the microgeometry of plate martensite for different reheating treatments. The trends in Fig. 7(a) and (b) show that the average plate size decreases with a decrease in PAGS. In a given microstructure, a wide range of sizes of martensite plates can be observed. Fisher et al. (Ref 21) formulated the austenite partitioning model for martensite growth kinetics where martensite units grow and divide austenite grains. New martensite units form in finer austenite constituents, and as a result, the mean martensite plate volume

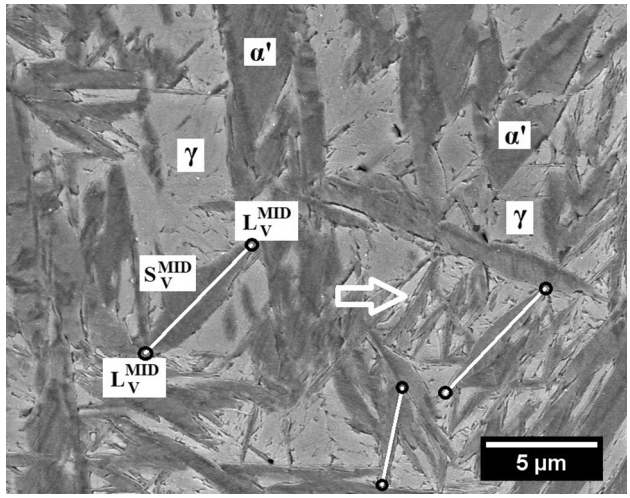

Fig. 6 Scanning electron micrograph of a reheat-quenched plate martensite and retained austenite microstructure etched with 2 pct nital. Constituents and stereological quantities are schematically labeled in the micrograph

Table 2 Summary of stereological measurements

Reheat temp. (in °C)	900	1000	1100
Experimental quantities			
PAGS, μm	12.4 ± 2.2	31.6 ± 3.6	69.8 ± 5.8
Stereological quantities			
V_V	0.72 ± 0.01	0.68 ± 0.03	0.72 ± 0.03
S_V^{MID}, μm^{-1}	1.21 ± 0.06	0.86 ± 0.06	0.71 ± 0.04
L_V^{MID}, μm^{-2}	1.1 ± 0.1	0.59 ± 0.05	0.41 ± 0.02
Morphological quantities			
t_{avg}, μm	0.59 ± 0.06	0.79 ± 0.07	1.01 ± 0.07
r_{avg}, μm	2.2 ± 0.24	2.92 ± 0.32	3.46 ± 0.25

decreases with increasing transformation. Martensite transformation in the "fill-in" mode initiates with uniform formation of martensite plates in all austenite grains, while the subsequent smaller plates form in the smaller austenite volumes partitioned by previously formed plates, resulting in relatively large values of the reported standard deviations in plate sizes (Ref 15). The white arrow in Fig. 6 points toward fine martensite plates that potentially partitioned a large RA constituent during the fill-in stage of the transformation. The mean radius of martensite midrib decreases with an increase in the number of units per grain as the transformation progresses (Ref 22).

Guimarães et al. (Ref 16) suggest that martensite formation proceeds in two steps: elastic spread of the martensite midrib followed by thickening of plates. PAGBs and martensite–austenite interfaces are obstacles to the elastic propagation of midribs. The average plate radius is geometrically limited by impingement against physical barriers (Ref 16). Furthermore, as the midrib lengthens, the deformation of austenite in the vicinity of the propagating front impedes its growth, limiting the length of plates (Ref 16).

The average plate thickness is greater at higher values of PAGS. As the martensite plate thickens, it deforms the surrounding austenite plastically. The surrounding austenite imposes a local mechanical constraint over the thickness of plates (Ref 16). The complex interplay of mechanical and

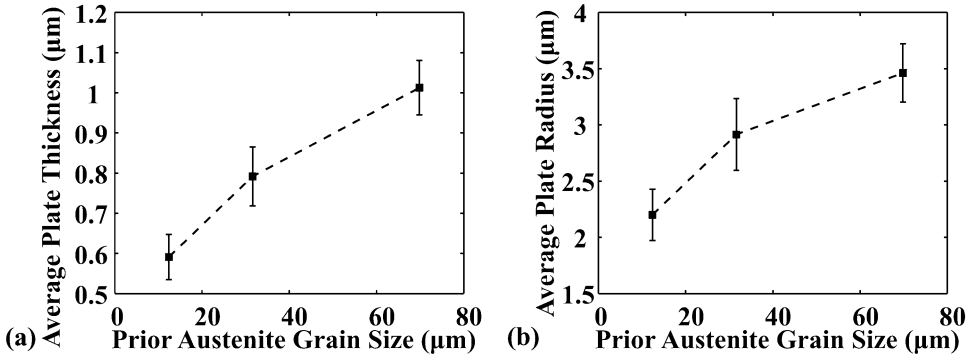

Fig. 7 Quantitative trends in morphology of plate martensite as a function of prior austenite grain size of reheated specimen: (a) average plate thickness and (b) average plate radius

geometrical constraints during martensite growth via thickening can potentially explain the trend observed in Fig. 7(b). Previous studies on martensitic transformations in high-carbon steels have shown that t_{avg} is composition dependent (Ref 22). Further, Chang et al. (Ref 14) reported that the values of t_{avg} are more sensitive to austenite grain size in O1 tool steel than in a Fe-1.4C-0.02P alloy. Chang et al. (Ref 23) reported t_{avg} and r_{avg} values close to 1 μm and 2 μm for a Fe-1.4C-0.02P alloy, which are near the range of values obtained in this investigation. Overall the growth of martensite and its morphology is limited by both characteristics of the austenite and the grain/phase boundary interfaces.

3.3 Thermal Cycling–Retained Austenite Size Distribution

Austenite grains are partitioned as the transformation progresses and a wide range of constituent sizes are obtained. Austenite regions were identified in 2-D micrographs and their circular equivalent diameters were determined. The Schwartz-Saltykov method was employed to calculate the volumetric RA constituent size distribution $(N_V)_i$ from the 2-D RA area sections (Ref 18). Figure 8 shows the trend in average RA constituent diameter as a function of PAGS. Figure 9(a-c) shows the frequency distribution for RA constituent sizes in RH900, RH1000, and RH1100 microstructures, respectively.

The average RA constituent diameter increases with an increase in prior austenite grain size of the microstructure. Since all the conditions have approximately the same volume fraction of RA, the influence of PAGS can be isolated in these conditions. The linear trend for average RA diameter can thus be primarily attributed to geometrically constrained spread of martensite in different PAGS. RA constituents share interfaces with plate martensite. As discussed in the previous section, finer PAGS results in finer martensite plates, and thus a greater surface area to volume ratio (S_V^{MID}). Therefore, finer RA constituents are found in fine PAGS microstructures.

The range of the sizes and the size of the largest austenite constituent increase with an increase in PAGS. In the existing literature pertaining to RA-containing advanced-high-strength-sheet (AHSS) steels, the stability of RA has been attributed to factors such as composition, size, shape, and strain partitioning in surrounding microstructures (Ref 24-26). The submicron constituents form the greatest fraction of RA, and they are potentially mechanically stable compared to the larger RA. The RA volume contribution for each size class interval was determined by multiplying the number fraction $(N_V)_i$, with the specific spherical volume (determined using the average

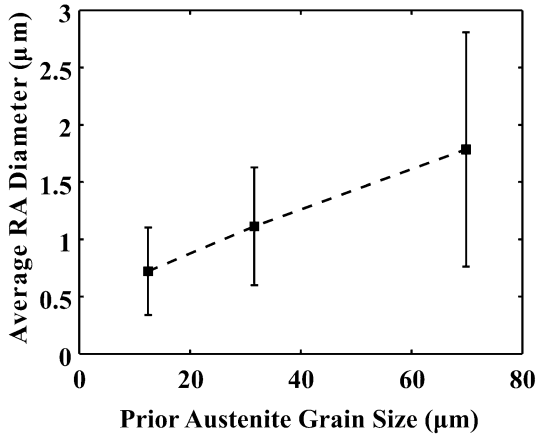

Fig. 8 Average equivalent diameter of the RA constituents as a function of prior austenite grain size (PAGS) of reheated specimen

diameter for the size class). The size distribution data suggest that constituents with diameter greater than 2.5 μm contribute to approximately 75 pct RA by volume in RH1100 and approximately 25 pct RA by volume in RH1000, while all the RA constituents in RH900 are finer than 2.5 μm. It is hypothesized that microstructural refinement from thermal cycling resulting in a fine distribution of RA constituents can consequently affect the mechanical behavior, e.g., fatigue.

3.4 Step Quenching

Figure 10 shows quantitative stereological results from the microstructures of nital-etched step-quenched specimens. The step-quenched condition, hereby referred to as SQ, has 38.1 pct RA while the direct-quenched sample RH1000 contains 32 pct RA. Both the RH1000 and SQ conditions had the same austenitizing cycle, and thus the PAGS is similar. It is to be noted that SQ underwent one reheating cycle (PAGS = 32.1 ± 1.1 μm), while RH1000 experienced two reheating cycles (PAGS = 31.1 ± 3.6 μm). A significant reduction in average plate radius and average plate thickness (as shown in Fig. 10a) suggests a refinement in martensite plate sizes. During quenching below the M_s temperature, formation of martensite deforms and introduces dislocations in the surrounding austenite due to the approximately 4 pct volume expansion and shear strains, which makes the plastic accommodation of subsequent martensite more difficult. Chatterjee and Bhadeshia (Ref 27) hypoth-

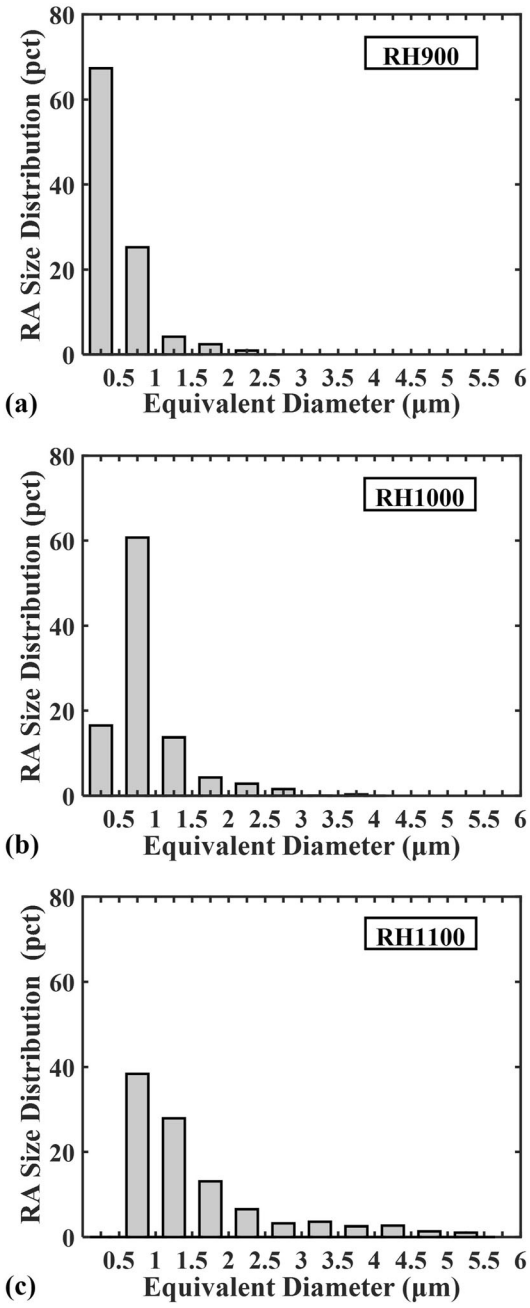

Fig. 9 Size distribution of RA constituents in reheated specimen: (a) RH900, (b) RH1000, and (c) RH1100. The number fraction of constituents is plotted against equivalent diameter

esize that the formation of dislocations in austenite interferes with glissile movement of martensite/austenite interfaces, and a plate stops growing when a strain is reached where the driving force for martensite formation (undercooling) equals the resistance to interface motion. During the second step, new plates of fresh martensite nucleate and grow in the deformed austenite. The deformed austenite has high density of defects which serve as nucleation sites for martensite. The presence of defects also increases the resistance to glissile motion of martensite-austenite interface during martensite growth. Hence, the subsequent transformation of the deformed-and-strengthened austenite results in finer martensite plates during quenching step 2.

The increase in volume fraction of RA for the step-quenched microstructure (Fig. 10b) as compared to the direct-quenched microstructure indicates stabilization of austenite. Dilatometry data for the step quenching process further supports the observation. Figure 11 shows the change in length (Δl) versus temperature data for SQ sample. Upon cooling the sample from 1000°C, the austenite thermally contracts. Between the M_s temperature, 142°C, and 100°C (primary quenching step), an increase in Δl is observed corresponding to the austenite to martensite transformation. During the isothermal holding at 100°C, the Δl increases by 0.5 μm. Apart from temperature homogenization, tempering of martensite and austenite decomposition can potentially cause the changes in length of the sample during isothermal holding. Upon further cooling, during the secondary quench step an initial drop in Δl is observed up until 87°C, after which, the sample starts expanding due to the transformation of RA to martensite, i.e., the M_s temperature in the remaining austenite after the first step is lower. Thus, the austenite is stabilized by the first quenching step. Seo et al. (Ref 28) also reported a shift in M_s temperature in dilatometry data during the formation of secondary martensite in quenching and partitioning (Q&P) processed advanced-high-strength steels, which contain lath martenisite and RA microstructures. This shift in M_s temperature was attributed to carbon enrichment in austenite during the partitioning step of the Q&P process (chemical stabilization). In another study, Van Bohemen et al. (Ref 5) studied the influence of partial bainitic transformation on the subsequent martensitic transformation in high-carbon 1080 steel. They observed a drop in M_s temperature due to prior bainite transformation, which was attributed to mechanical stabilization, wherein the shape change associated with the displacive bainite transformation plastically deforms and strengthens the austenite. The increased strength of austenite leads to a need for higher driving force for subsequent martensite formation and thus a lower M_s temperature for secondary martensite.

Further investigation of interrupted quenching of 52100 steel is required to determine the exact mechanism of austenite stabilization investigated. Like PAGS refinement, austenite stabilization may impact fatigue performance. The presence of RA in the microstructure enhances its ability to accommodate plastic strains (Ref 2). Additionally, under sufficient stress, RA transforms to martensite accompanied by volume expansion, that resists crack growth during fatigue loading (Ref 2). Man et al. (Ref 29) show that the stress required to induce phase transformation in an austenite constituent increases with a decrease in austenite size, indicating that the finer RA constituents are mechanically more stable. It is therefore hypothesized that a fine distribution and increased amount of RA constituents, resulting from step quenching, can consequently affect the mechanical behavior, e.g., fatigue.

4. Summary and Conclusions

Microstructure development during thermal cycling and step quenching of commercial high-carbon 52100 steel was investigated with the following highlights and conclusions:

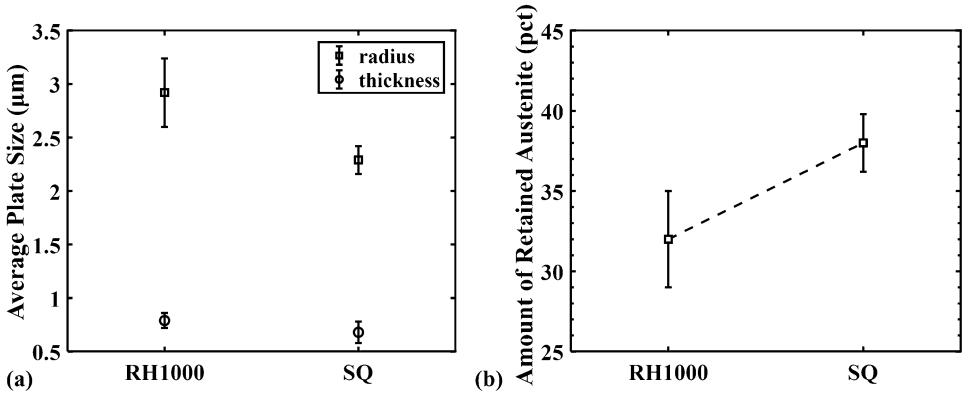

Fig. 10 Comparison of stereological parameters on direct-quenched and step-quenched microstructures: (a) RA volume fraction and (b) plate martensite size

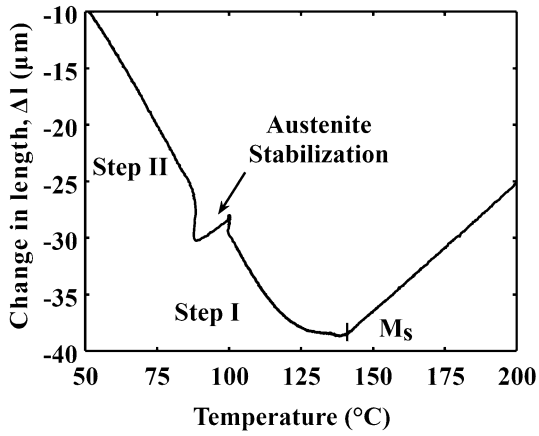

Fig. 11 Change in length vs. temperature dilatometry data for the cooling segment of step quenching at 100 for 1000 s

- Thermal cycling heat treatment is an effective approach for PAGS control. During reheating above A_3 temperature, low temperatures, and short isothermal holdings resulted in the greatest grain size refinement.
- Multiple reheating cycles did not substantially reduce the PAGS further. However, a narrower PAGS distribution was obtained, potentially resulting in a reduced number of large intergranular crack nucleation sites in fatigue.
- The average martensite plate radius and plate thickness increase with increase in PAGS. The growth of martensite and its morphology are limited by physical obstacles such as grain/phase boundary interfaces.
- Stereological measurements on plate martensite and RA constituents showed that finer PAGS leads to finer plates and RA constituents. Since the mechanical stability of austenite depends on its size, grain refinement can potentially lead to a more stable retained austenite in carburized components.
- Interrupted quenching below the M_s temperature results in stabilization of austenite (mechanical and/or chemical) and a refinement of martensite plates. Finer martensite along with higher amounts of RA can potentially improve the mechanical performance of carburized components in service.

Acknowledgments

This research project is being supported by NSF-CMMI award number 1728007. The authors also gratefully acknowledge the support of the sponsors of Advanced Steel Processing and Products Research Center at Colorado School of Mines, especially TimkenSteel, for providing the raw material for this investigation.

References

1. H. Mohrbacher, Metallurgical Concepts for Optimized Processing and Properties of Carburizing Steel, *Adv. Manuf.*, 2016, **4**, p 105–114. https://doi.org/10.1007/s40436-016-0142-9
2. G. Krauss, Fatigue and Fracture, in *ASM Handbook.Vol.19*, ASM International, pp. 680–690, (1996). https://doi.org/10.31399/asm.hb.v19.9781627081931
3. J.P. Wise and D.K. Matlock, Bending Fatigue of Carburized Steels: A statistical Analysis of Process and Microstructural Parameters, *SAE Trans.*, 2000, **109**, p 182–191. https://doi.org/10.4271/2000-01-0611
4. C.A. Apple and G. Krauss, Microcracking and Fatigue in a Carburized Steel, *Metall. Trans.*, 1973, **4**(5), p 1195–1200. https://doi.org/10.1007/BF02644511
5. S.M.C. Van Bohemen and J. Sietsma, Martensite Formation in Partially and Fully Austenitic Plain Carbon Steels, *Metall. Mater. Trans. A*, 2009, **40**(5), p 1059–1068. https://doi.org/10.1007/s11661-009-9796-2
6. S.M.C. van Bohemen and J. Sietsma, Kinetics of Martensite Formation in Plain Carbon Steels: Critical Assessment of Possible Influence of Austenite Grain Boundaries and Autocatalysis, *Mater. Sci. Technol.*, 2014, **30**(9), p 1024–1033. https://doi.org/10.1179/1743284714Y.0000000532
7. A.R. Entwisle, The Kinetics of Martensite Formation in Steel, *Metall. Trans.*, 1971, **2**(9), p 2395–2407. https://doi.org/10.1007/BF02814877
8. C.H. Shih, B.L. Averbach, and M. Cohen, Some Characteristics of the Isothermal Martensitic Transformation, *JOM*, 1955, **7**(1), p 183–187. https://doi.org/10.1007/BF03377476
9. G.B. Olson and M. Cohen, A General Mechanism of Martensitic Nucleation: Part I. FCC → HCP and Other Martensitic Transformations, *Metall. Trans. A*, 1976, **7**, p 1897–1904. https://doi.org/10.1007/bf02659822
10. G.B. Olson and M. Cohen, A General Mechanism of Martensitic Nucleation: Part II. FCC → BCC and other Martensitic Transformations, *Metall. Trans. A*, 1976, **7**, p 1905–1914. https://doi.org/10.1007/bf02659823
11. S. Karewar, J. Sietsma, and M.J. Santofimia, Effect of Pre-existing Defects in the Parent fcc Phase on Atomistic Mechanisms During the Martensitic Transformation in pure Fe: a Molecular dynamics Study, *Acta Mater.*, 2018, **142**, p 71–81. https://doi.org/10.1016/j.actamat.2017.09.049

12. C. Celada-Casero, J. Sietsma, and M.J. Santofimia, The Role of the Austenite Grain Size in the Martensitic Transformation in Low Carbon Steels, *Mater. Des.*, 2019, **167**, p 107625. https://doi.org/10.1016/j.matdes.2019.107625
13. D.V. Edmonds, K. He, F.C. Rizzo, B.C. De Cooman, D.K. Matlock, and J.G. Speer, Quenching and Partitioning Martensite—A Novel Steel Heat Treatment, *Mat. Sci. Eng. A*, 2006, **438–440**, p 25–34. https://doi.org/10.1016/j.msea.2006.02.133
14. P.H. Chang, P.G. Winchell, and G.L. Liedl, Quantitative Geometric Characterization of High Carbon Martensite, *Metall. Trans. A*, 1983, **14**(1), p 163–173. https://doi.org/10.1007/BF02651612
15. P.R. Rios and J.R.C. Guimarães, Microstructural Path Analysis of Athermal Martensite, *Scr. Mater.*, 2007, **57**(12), p 1105–1108. https://doi.org/10.1016/J.SCRIPTAMAT.2007.08.019
16. J.R.C. Guimarães and P.R. Rios, Spatial Aspects of Martensite, *Metall. Mater. Trans. A*, 2012, **43**(7), p 2218–2224. https://doi.org/10.1007/s11661-012-1102-z
17. J.R.C. Guimarães and J.C. Gomes, A Metallographic Study of the Influence of the Austenite Grain Size on Martensite Kinetics, *Acta Metall.*, 1978, **26**(10), p 1591–1596. https://doi.org/10.1016/0001-6160(78)90068-8
18. E.E. Underwood, Quantitative Stereology for Microstructural Analysis, *Microstructural analysis*, Springer, Boston, 1973, p 35–66 https://doi.org/10.1007/978-1-4615-8693-7_3
19. R.T. DeHoff and F.N. Rhines, *Quantitative MIcroscopy*, McGraw-Hill, New York, 1968
20. J. Takahashi and H. Suito, Evaluation of the Accuracy of the Three-dimensional Size Distribution Estimated from the Schwartz-Saltykov Method, *Metall. Mater. Trans. A*, 2003, **34**, p 171–181. https://doi.org/10.1007/s11661-003-0218-6
21. J.C. Fisher, J.H. Hollomon, and D. Turnbull, Kinetics of the Austenite → Martensite Transformation, *JOM*, 1949, **1**(10), p 691–700
22. J.R.C. Guimarães, Athermal Martensite: Genesis of Microstructure and Transformation Curves, *Mater. Sci. Eng., A*, 2008, **476**(1–2), p 106–111. https://doi.org/10.1016/j.msea.2007.04.068
23. P.H. Chang, H. Rubin, P.G. Winchell, and G.L. Liedl, The Determination of Size Distribution of Martensite Plates by Kernel Estimation, *Scr. Metall.*, 1982, **16**(5), p 531–536. https://doi.org/10.1016/0036-9748(82)90264-2
24. I.B. Timokhina, P.D. Hodgson, and E.V. Pereloma, Effect of Microstructure on the Stability of Retained Austenite in Transformation-induced-plasticity Steels, *Metall. Mater. Trans. A*, 2004, **35**(8), p 2331–2341. https://doi.org/10.1007/s11661-006-0213-9
25. J.H. Ryu, D.-I. Kim, H.S. Kim, H.K.D.H. Bhadeshia, and D.-W. Suh, Strain Partitioning and Mechanical Stability of Retained Austenite, *Scr. Mater.*, 2010, **63**(3), p 297–299. https://doi.org/10.1016/J.SCRIPTAMAT.2010.04.020
26. S. Zhang and K.O. Findley, Quantitative Assessment of the Effects of Microstructure on the Stability of Retained Austenite in TRIP Steels, *Acta Mater.*, 2013, **61**(6), p 1895–1903. https://doi.org/10.1016/j.actamat.2012.12.010
27. S. Chatterjee and H.K.D.H. Bhadeshia, Transformation Induced Plasticity Assisted Steels: Stress or Strain Affected Martensitic Transformation, *Mater. Sci. Technol.*, 2007, **23**(9), p 1101–1104
28. E.J. Seo, L. Cho, Y. Estrin, and B.C. De Cooman, Microstructure-Mechanical Properties Relationships for Quenching and Partitioning (Q&P) Processed Steel, *Acta Mater.*, 2016, **113**, p 124–139. https://doi.org/10.1016/j.actamat.2016.04.048
29. T. Man, T. Ohmura, and Y. Tomota, Mechanical Behavior of Individual Retained Austenite Grains in High Carbon Quenched-tempered Steel, *ISIJ Int.*, 2019, **59**(3), p 559–566. https://doi.org/10.2355/isijinternational.ISIJINT-2018-620